EES Solar

PAPER

View Article Online
View Journal

Cite this: DOI: 10.1039/d5el00203f

Porphyrin–thieno[3,2-*b*]thiophene hole-transport materials enabling the production of long-lived radical ion pairs and high-performance perovskite solar cells

Ram R. Kaswan, [a] Bommaramoni Yadagiri,[bc] Jairam Tagare,[b] Vinay Kumar,[bc] Manne Naga Rajesh,[bc] Paul A. Karr,[d] L. Giribabu, *[bc] Surya Prakash Singh *[bc] and Francis D'Souza *[a]

Porphyrin-based hole-transporting materials (HTMs) have gained significant attention in perovskite solar cells (PSCs) due to their high efficiency, long-term stability, and excellent charge-transport properties. In this work, we reported a novel zinc porphyrin-based HTM denoted as SPS-PPY-TT for highly efficient and stable PSCs. The molecular design strategy of SPS-PPY-TT involves zinc porphyrin as the central core unit, which is functionalized with 6-fluoro-benzothiadiazole (FBDT) and hexylthieno[3,2-*b*] thiophene (TT) groups through an ethynyl linkage. The synthesised HTM was comprehensively investigated by using optical absorption spectroscopy, electrochemical methods, and theoretical studies. These studies indicate that the highest occupied molecular orbital (HOMO) energy levels are aligned with the valence band of $MAPbI_3$ perovskite. As a result, planar PSC devices constructed with SPS-PPY-TT as the HTM exhibit a power conversion efficiency (PCE) of 15.29%, while PSC devices made with Spiro-OMeTAD exhibit a PCE of 16.62%. The similar photovoltaic performance of SPS-PPY-TT and Spiro-OMeTAD might be attributed to the appropriate band alignment, higher hole mobility, and conductivity of SPS-PPY-TT. This work demonstrates that TT is an alternative methoxy-free donor for porphyrin HTMs to achieve highly efficient and stable PSCs. Eventually, the same molecular system, which was axially coordinated with ImC_{60}, was utilised to generate a long-lived charge-separated species with a lifetime of 1.56 ns after irradiation at different wavelengths. The value of k_{CS}/k_{CR} was found to be 5.78, revealing charge stabilisation.

Received 4th December 2025
Accepted 26th January 2026

DOI: 10.1039/d5el00203f

rsc.li/EESSolar

Broader context

The hole-transporting layer (HTL) is one of the essential components of perovskite solar cells (PSCs) for achieving high efficiency. Despite the certified device efficiency of 26.7% using a single-junction architecture, perovskite-silicon tandem cells have reached record efficiencies of 34.85%, but the technology is not yet commercialized due to the unstable Spiro-OMeTAD-based HTL. Porphyrins are the best alternative HTLs, owing to their electron-rich nature, easy tunability of their energy levels, strong π–π stacking, and high thermal and photochemical stability. Porphyrins in the donor–π–donor concept have enhanced the π-electron cloud on the porphyrin plane and facilitate hole exchange with the perovskite layer. The introduction of long alkoxy groups at the *ortho*-position of the *meso*-phenyl ring enhances the hydrophobicity of the HTL layer, thereby improving the device's moisture resistance. The high hole mobility of porphyrin-based HTMs does not require any additives, which also enhances device durability. PSCs using porphyrin-based HTLs have demonstrated device efficiencies of >20%, and device durability has also improved significantly. This will not only reduce device cost but also provide scope for the near-term commercialization of the technology.

Introduction

In recent years, hybrid organic–inorganic perovskite solar cells have garnered significant attention due to their high power conversion efficiency (PCE) and simple, low-cost fabrication process.[1–3] Since the first report of a PCE of 3.8% in 2009, PSC efficiency has exceeded 26%.[4] Although PSCs have achieved remarkably high efficiency, commercialization remains difficult due to unresolved fabrication challenges, environmental

[a]*Department of Chemistry, University of North Texas, Denton, Texas 76203-5017, USA. E-mail: francis.dsouza@unt.edu*

[b]*Department of Polymers and Functional Materials, CSIR-Indian Institute of Chemical Technology, Uppal Road, Tarnaka, Hyderabad-500007, India. E-mail: giribabu.iict@csir.res.in; spsingh.iict@csir.res.in*

[c]*Academy of Scientific and Innovative Research (AcSIR), Ghaziabad- 201002, India*

[d]*Department of Physical Sciences and Mathematics, Wayne State College, 111 Main Street, Wayne, NE 68787, USA*

toxicity, unstable hole and electron transporting materials, and poor long-term stability. Additionally, selecting appropriate, high-quality hole transporting materials (HTMs) is essential for creating highly stable and efficient PSC devices.[5–7]

Currently, high-performance n-i-p structured PSCs often use the small molecule 2,2′,7,7′-tetrakis(*N*,*N*-di-(*p*-methoxyphenyl) amino)-9,9′-spirobi-fuorene (Spiro-OMeTAD) as the HTM because of its suitable energy levels, amorphous nature, high solubility, and ease of processing.[8] However, Spiro-OMeTAD has several disadvantages, including high cost, limited hole mobility, low conductivity, and a lengthy synthesis process.[9,10] Moreover, its low hole mobility and conductivity require chemical doping with p-type dopants and additives, such as *tert*-butyl pyridine (*t*-BP), lithium bis-(trifluoromethanesulfonyl) imide (Li-TFSI), and cobalt complexes (FK209) to improve device performance. However, the hygroscopic nature of these dopants can negatively impact long-term device stability, potentially limiting broader application in PSCs.[11–13] Therefore, there is a strong need to develop efficient, cost-effective novel HTMs as alternatives to Spiro-OMeTAD.[14–21]

Porphyrin derivatives show great potential as HTMs because of their highly electron-rich nature, good thermal and photochemical stability, and strong π–π stacking.[22] Additionally, their energy levels can be tuned by modifying the molecular structure to optimize hole injection. Several research groups have reported porphyrin-based small molecular derivatives as HTMs for PSCs.[23–26] Planar porphyrin-based HTMs with a donor–π–donor (D–π–D) structure have attracted considerable attention for their PCE and device durability. Hwan Kyu Kim *et al.*[24] developed novel D–π–D structured, π-extended porphyrin-based HTMs (SGT-061, SGT-062, and SGT-063) with triarylamine donor units. One porphyrin HTM features a less bulky donor (SGT-061), which results in higher hole mobility and strong π–π stacking between molecules. Consequently, PSCs made with this HTM demonstrate better photovoltaic performance than those with bulkier HTMs (SGT-062 and SGT-063).[24]

Peter Chen *et al.*[26] reported a series of porphyrin-dopant-free HTMs (Y2 and YZT4) containing zinc(II) porphyrin cores and ethynylarene groups for PSCs. These HTMs are simple in structure, easily accessible, and can be synthesized in two steps with good yields. The doped YZT4 HTM achieves a high PCE of 14.95% in TiO_2-based PSCs and exhibits fair stability compared to Spiro-OMeTAD-based devices.[26] Recently, L. Giribabu *et al.* developed triphenyl imidazole-substituted D–π–D structured, dopant-free porphyrin HTMs for perovskite solar cells. All these HTMs were characterized using various spectroscopic and electrochemical methods. Among them, the CuLD HTM exhibits higher conductivity, better hole mobility, and appropriate energy band alignment with $MAPbI_3$ perovskite, leading to a PCE of 12.44%.[25]

Small molecular/polymer materials containing thieno[3,2-*b*] thiophene (TT) and 6-fluoro-benzothiadiazole (FBDT) are well-investigated in the fields of field-effect transistors (FETs), dye-sensitized solar cells, and organic photovoltaics (OPVs).[16,27–29] The strong electron-donating and self-assembly properties of the TT unit strongly influence the electronic structure of semiconducting materials.[30] Furthermore, incorporating the electronegative FBDT unit can significantly affect the HOMO and LUMO energy levels of the semiconductors by extending the π-conjugation, which also improves planarity and charge transport. In this study, we designed and synthesized a D–π–D type zinc porphyrin-based HTM called SPS-PPY-TT. This molecule consists of zinc porphyrin as the central core, functionalized with FBDT and hexylthieno[3,2-*b*]thiophene groups *via* an ethynyl linkage. The FBDT acts as a weak acceptor and π-space unit, reducing the HOMO energy level of SPS-PPY-TT by extending the π-conjugation. The ethynyl linkage enhances the molecule's coplanarity while improving charge transport. Additionally, the donor HTT unit, with an n-hexyl alkyl chain, enhances solubility and stability compared to methoxy-substituted donor groups. As a result, $MAPbI_3$-based PSC devices incorporating SPS-PPY-TT as the HTM achieved a PCE of 15.29%, owing to favourable band alignment, higher hole mobility, and conductivity, and improved HTM/perovskite interface quality. This work demonstrates that HTT can serve as an effective methoxy-free donor in porphyrin HTMs to produce highly efficient zinc porphyrin-based PSCs.

Besides mimicking natural photosynthesis for light harvesting, a self-assembled synthetic model composed of SPS-PPY-TT and imidazole-functionalized fullerene (ImC_{60}) was developed. A key goal in this research field is to create artificial light-harvesting systems that can absorb light, transfer the excitation energy to an energy sink, and utilize this energy for photoinduced electron transfer (PET).[31–42] Several elegant molecular architectures, including ImC_{60} and zinc porphyrin, have been designed and studied.[43–50] In this work, our primary objective is to employ a supramolecular approach to create a combined model system and investigate electron transfer upon photoexcitation. Instead of using a simple porphyrin that absorbs light mainly in the 415–430 nm (Soret band) and 550–600 nm (Q bands) and emits in the 600–660 nm range, we targeted a broad-band light-absorbing system, extending from 300–800 nm (UV-Vis-NIR) and emitting between 600 and

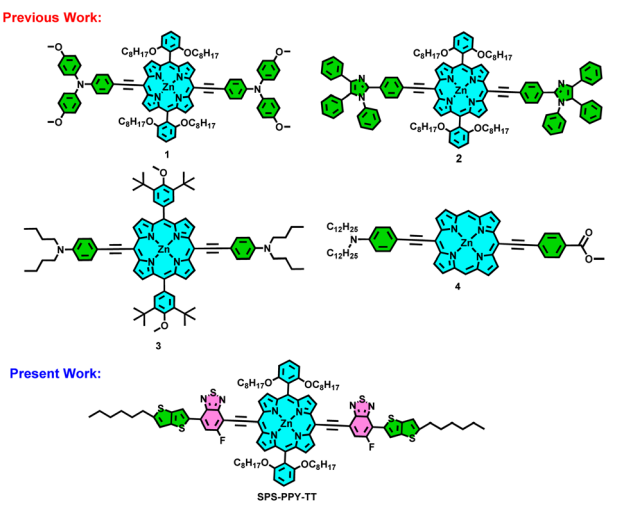

Scheme 1 Present and previous studies on porphyrin hole transporting materials for PSCs.

900 nm. This NIR-extended porphyrin design aims to confirm that excitation in the NIR range can generate a long-lived charge-separated (CS) state, enabling better utilization of the solar spectrum. Implementing broadband light-absorbing chromophores that mimic natural photosynthetic systems can significantly enhance photon absorption and facilitate charge separation over a wide wavelength range (Scheme 1).

Results and discussion

Synthesis

The synthetic procedure for the SPS-PPY-TT HTM molecule is presented in Scheme S1, along with characterization and purification details provided in the SI (Fig. S1–S8). Intermediates I, II, and V were synthesized according to previously reported literature.[28,51] The Sonogashira coupling reaction between intermediate II and (triisopropylsilyl)acetylene, using $Pd(PPh_3)_2Cl_2$ as the catalyst and triethylamine (Et_3N), produced intermediate III. Deprotection with TBAF then yielded intermediate IV in good yield. Subsequently, intermediates IV and V underwent Sonogashira coupling to produce the targeted final product, SPS-PPY-TT, in good yields. All intermediates and final products were purified *via* column chromatography and characterized by ^1H NMR and mass spectrometry. SPS-PPY-TT exhibits good solubility in various organic solvents, including dichloromethane (DCM), dimethyl sulfoxide (DMSO), ethyl acetate (EtOAc), dimethylformamide (DMF), and chloroform ($CHCl_3$).

Spectroscopic studies

The optical results of the newly synthesized compound in solution as well as in the solid phase (thin film) are displayed in Fig. 1, and their photophysical data are summarized in Table 1. Irrespective of the medium, SPS-PPY-TT covered a wide range of absorption, spanning from 300 to 800 nm, showing its visible-to-far red light-harvesting potential. The broadband light capturing ability could be attributed to the presence of thiophene substituents at the *meso* position, which extends the π-conjugation. In the solution phase, SPS-PPY-TT was characterized by an intense and broad Soret band located at 380–550 nm and a pair of strong Q-bands between 550 and 750 nm, as shown in Fig. 1a. The onset absorption wavelength (λ_{onset}) was utilized to calculate the optical band gap ($E_g^{opt} = 1240/\lambda_{onset}$) of SPS-PPY-TT, and it was found to be 1.58 eV. In the case of the solid state, a substantial change in spectral features was noted in the absorption spectrum. Broadening and a significant red shift of 50 nm were observed as compared to those in the solution phase, suggesting the generation of J-aggregates in the solid state. And usually, such aggregations trigger a strong intermolecular π–π stacking, which is expected to enhance the hole mobility and is exceptionally useful for the light-harvesting applications in the visible-to-near-infrared region.

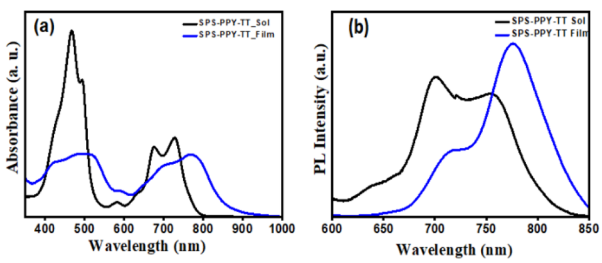

Fig. 1 (a) Absorption spectra and (b) emission spectra of SPS-PPY-TT in THF solvent and thin film state.

Fig. 1b exhibits the emission spectra of the same compound measured at room temperature. Two emission bands were seen when the compound was excited at the Soret band. Zinc porphyrin (ZnTPP) molecules are well known for emitting light in the visible region. However, due to the presence of large substituents with heteroatoms, they are responsible for near-infrared emission in the SPS-PPY-TT molecule. The SPS-PPY-TT emission spectrum exhibits a similar trend to its Q-band absorption spectrum, with a red shift of nearly 50 nm observed at 790 nm. To investigate intramolecular charge transfer (ICT), solvatochromic experiments were performed by varying the polarity of the utilized solvents. Fig. S9 presents the photoluminescence (PL) spectra of SPS-PPY-TT in toluene, tetrahydrofuran, and acetonitrile. Upon increasing the solvent polarity, a red shift was observed for the emission bands, which suggests the presence of excited-state charge transfer signals.

Formation and characterization of donor–acceptor conjugates

Fig. 2 shows the SPS-PPY-TT's absorption and fluorescence titration results during ImC_{60} binding. Upon the addition of 0.5 mM of ImC_{60} to a solution of SPS-PPY-TT in a series, changes in optical spectra disclosed the spectral characteristics of penta-coordinated zinc porphyrin, *i.e.*, it demonstrated red-shifted Soret and visible absorption signals with the appearance of isosbestic points.[53] A slight red shift of the Soret band, a diminishing of the intensity of the visible band at 675 nm, and the presence of a distinct isosbestic point at 692 nm produced a new signal at 712 nm (Fig. 2a). The spectral intensity modifications of the visible band were used to establish a Benesi–Hildebrand plot, as depicted in Fig. 2b.[54] The binding constant

Table 1 Optoelectronic properties of SPS-PPY-TT in solution and thin film states

	Optical properties				Electrochemical properties (*vs.* Fc/Fc^+)		
HTM	λ_{abs} solution (nm)	λ_{abs} film (nm)	λ_{onset} (nm)	E_g (eV)	E_{ox} (eV)	E_{red} (eV)	$\Delta E_{1/2}$ (eV)
SPS-PPY-TT	729	776	780	1.58	0.35, 0.67, 1.12	−1.67, −1.77, −1.93, −2.17, −2.54	2.03
SPS-PPY-TT: ImC_{60}	—	—	—	—	0.35, 0.67, 1.16	−1.30, −1.66, −1.76, −2.17, −2.76	1.61

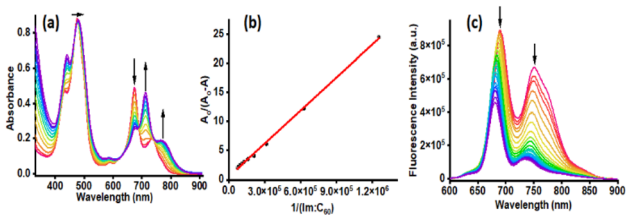

Fig. 2 (a) Absorption titration studies of SPS-PPY-TT with increasing amounts of 0.5 mM ImC_{60} across a series of additions. (b) The Benesi–Hildebrand plot is used to evaluate the binding constant. (c) Fluorescence titration studies of SPS-PPY-TT excited at the Soret band (436 nm) with increasing additions of ImC_{60} in *o*-DCB.

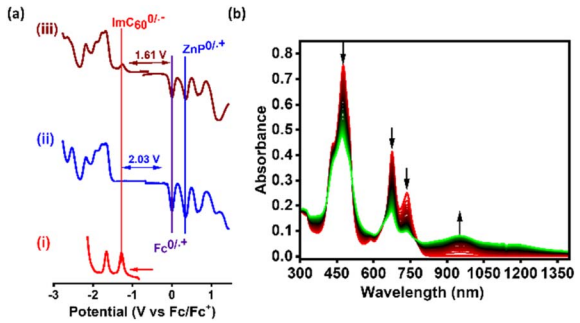

Fig. 3 (a) DPVs of (i) ImC_{60}, (ii) SPS-PPY-TT, and (iii) SPS-PPY-TT:ImC_{60} (shifting of the reduction potential is shown by a red vertical line), and (b) spectral changes during the first oxidation in *o*-DCB containing 0.1 M TBA(ClO_4) electrolyte.

(*K*) for the formation of an axially connected supramolecular assembly (SPS-PPY-TT:ImC_{60}) was found to be 2.8×10^4. This value closely matches the earlier reported values. The relatively high value of K suggests that a stable, coordinated, attached donor–acceptor system is being formed in the solution. Additionally, the emission spectrum of SPS-PPY-TT was also tracked throughout the titration studies. As shown in Fig. 2c, substantial quenching was seen in emission bands upon increasing the addition of ImC_{60}, which suggested the occurrence of excited-state events, possibly an electron transfer from the excited state of porphyrin to ImC_{60}.

Electrochemical studies

Next, to gather vital information for drawing a Jablonski-type energy diagram to observe different photoevents and their thermodynamic feasibility upon photoexcitation, electrochemical studies were conducted, as they provide valuable insights into redox properties. Fig. 3a displays the differential pulse voltammetry curves of the control compound ImC_{60}, SPS-PPY-TT, and SPS-PPY-TT: ImC_{60} with the ferrocene/ferrocenium (Fc/Fc^+) couple as an internal reference in a dry *o*-dichlorobenzene solution containing 0.1 M tetrabutylammonium perchlorate (TBA) ClO_4 as the supporting electrolyte. These experiments were carried out under a nitrogen atmosphere, and the results obtained are presented in Table 1. As reported earlier, under the applied potential window, ImC_{60} exhibited five distinct reversible reduction waves at −1.30, −1.66, −1.76, −2.17, and −2.76 V *vs.* Fc/Fc^+. In comparison, SPS-PPY-TT shows three consecutive reversible oxidation redox waves at 0.35, 0.67, and 1.12 V and five reversible reduction waves at −1.67, −1.77, −1.93, −2.17, and −2.54 V. The addition of ImC_{60} to SPS-PPY-TT resulted in a significant anodic shift of 410 mV during the first reduction process, indicating that this reduction occurred because of the presence of ImC_{60}. The facile reduction of SPS-PPY-TT:ImC_{60} accounts for a significantly smaller redox gap than E_{00} (1.74 eV), showing the thermodynamic feasibility of the charge separation process upon photoexcitation, making it a potential candidate for light-harvesting applications (the calculated redox gaps are indicated by an arrow in Fig. 3a). The reversibility of redox waves was confirmed using cyclic voltammograms, as shown in Fig. S10. Furthermore, spectroelectrochemical experiments were performed in an optically transparent thin-layer cell to monitor the modification of optical spectra during the first oxidation of SPS-PPY-TT, as illustrated in Fig. 3b. During this process, the decrease in the intensities of the neutral compound's peaks, located at 475, 675, and 736 nm, resulted in the generation of a new broad peak at 950 nm. The origin of this new signal can be attributed to the formation of the radical cation, $ZnP^{\bullet+}$. Additionally, several isosbestic points were detected, located at 409, 512, 641, and 781 nm.

Theoretical studies

Next, density functional theory (DFT) calculations were performed using the Gaussian 09 program to gain further insights into the structural, electronic, and charge-transport properties of SPS-PPY-TT. The results from these studies are shown in Fig. 4.[55] The ground state geometry optimization was conducted at the CAM-B3LYP 6-311 g(d,p) level, revealing that the porphyrin macrocycle and *meso*-substituent (FBDT and TT) units are coplanar.

This planarity promotes a tightly packed molecular conformation as discussed earlier in the optical results. Similarly, the alkyl chains attached to TT and phenyl units are twisted out of the plane, which helps enable the solubility of SPS-PPY-TT in common organic solvents. Furthermore, molecular electrostatic

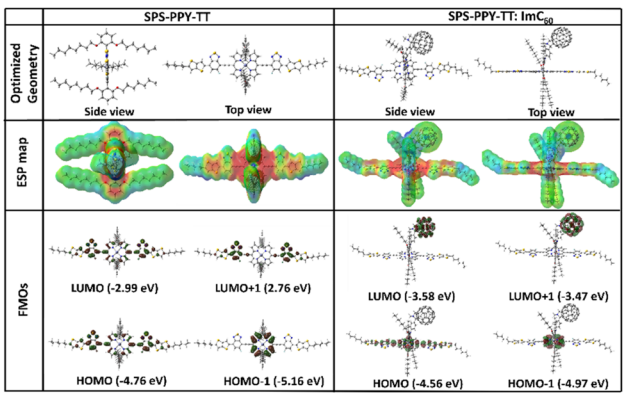

Fig. 4 CAM-B3LYP/6-311G (d,p) optimized structures, both side and top views (top row), molecular electrostatic potential map (middle row), and the frontier molecular orbitals (FMOs, bottom row) for SPS-PPY-TT (first column) and SPS-PPY-TT:ImC_{60} (second column).

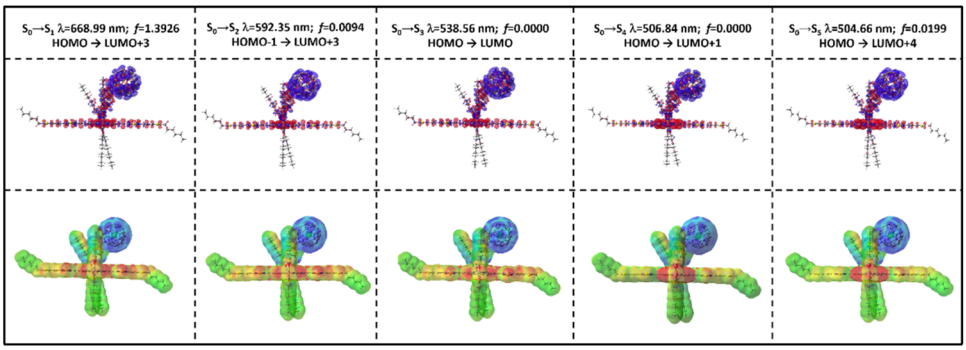

Fig. 5 Hole–electron isosurfaces and the charge density difference maps of SPS-PPY-TT:ImC$_{60}$ (red: charge donor, blue: charge acceptor; -2.000×10^{-5} V to 2.000×10^{-5} V).

potential (MEP) maps were generated to illustrate charge distribution and identify sites favorable for the charge transfer (CT) process. These maps also help examine donor–acceptor interactions and provide insights into photophysical behavior. In the case of SPS-PPY-TT, the MEP showed a positive electrostatic potential (red color) on the porphyrin core and a weak negative potential (blue color) on the *meso* substituents. For SPS-PPY-TT:ImC$_{60}$, the positive potential remained at the same moiety, whereas the negative potential was observed on the ImC$_{60}$ group. These results suggest a push–pull effect from porphyrin to *meso* substituents and ImC$_{60}$ in SPS-PPY-TT and SPS-PPY-TT: ImC$_{60}$, respectively.

The bottom row shows the frontier molecular orbitals (FMOs) of the newly synthesized molecules. In the case of SPS-PPY-TT, the HOMO and LUMO are mainly localized on the porphyrin moiety and partially extend to the thieno substituent rings. Additionally, the HOMO−1 is mainly confined to the porphyrin, while the LUMO+1 is primarily on the FBDT substituents. The calculated energy gap is 1.77 eV, closely matching the experimental value.

Conversely, for SPS-PPY-TT:ImC$_{60}$, as expected, the LUMO and LUMO+1 are strongly localized on ImC$_{60}$, while the HOMO appears on the porphyrin ring and slightly extends to the substituents. The HOMO−1 for this molecule is completely localized on the central porphyrin moiety. These results show that ImC$_{60}$ acts as a strong electron acceptor, and the porphyrin ring functions as a donor in this supramolecular assembly.

Next, the ground state optimized output files were analyzed with TD-DFT to gain further insight into the vertical electronic transitions between the ground state and high-energy excited states, focusing on the first five excited states.[52] The results for the SPS-PPY-TT molecule are shown in Fig. S11, including the involved orbitals, wavelength, and oscillator strength for these transitions. The first four states demonstrate the occurrence of charge transfer (CT), with the hole (red) localized on the porphyrin and the electron (blue) on the thieno substituents. This strongly supports earlier experimental findings of CT, as explored through solvent studies. The fifth excited state may be attributed to a pure Frenkel state. These results are corroborated by FMOs and the ESP map, as previously discussed. Similarly, Fig. 5 presents the excited state results for the SPS-PPY-TT:ImC$_{60}$ system, clearly indicating that all five states can generate a hole–electron pair.[56,57] The top row shows the hole–electron isosurfaces, with the hole remaining on the porphyrin part and the electron located on the fullerene. The bottom row displays the electrostatic potential surfaces generated by taking the difference between the electron densities of the ground and excited states. TD-DFT calculations strongly suggest effective charge transfer from the porphyrin (donor) to the fullerene (acceptor), indicating that efficient photoinduced charge separation is expected upon photoexcitation. The theoretical UV-Vis spectrum, generated from TD-DFT, is provided in Fig. S12. A close resemblance to the experimental spectrum was observed with a split Soret band, located at 377 and 471 nm. In addition, a broad weak band spanning from 560–800 nm, centered at 636 nm, was also detected with a comparatively low oscillator strength, suggesting a less allowed transition, which could be attributed to the Q bands observed in the same region during

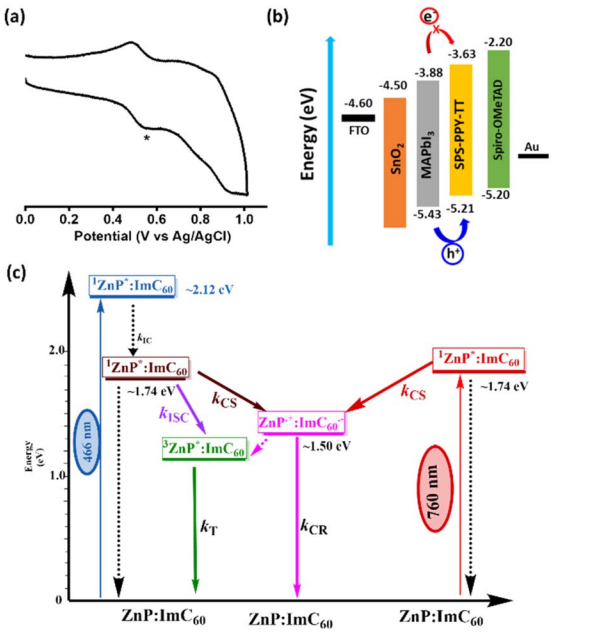

Fig. 6 (a) Cyclic voltammetry of SPS-PPY-TT in DCM solution with TBAF as electrolyte. (b) The energy level comparison of SPS-PPY-TT with MAPbI$_3$ perovskite. (c) Jablonski-type energy profile diagram showing all potential events upon photoexcitation.

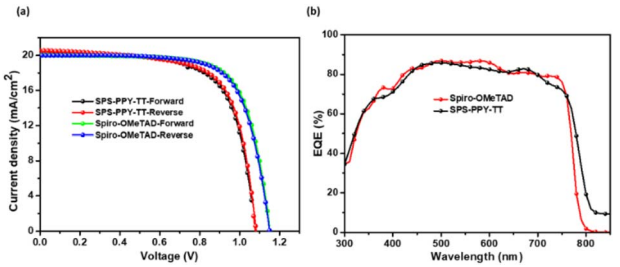

Fig. 7 (a) J–V characteristics and (b) EQE of Spiro-OMeTAD and SPS-PPY-TT-based PSCs.

the experimental studies. From theoretical investigations, it can be concluded that a close correspondence between the experimental and theoretical spectra indicates that the choice of functional and basis sets is reliable for comparison and contrast.

Energy profile diagram

For comparison and to ensure consistency with previously published results, a cyclic voltammogram of SPS-PPY-TT was also recorded in DCM solvent using ferrocene as an internal reference (Fig. 6a). The first oxidation potential was observed at 0.41 V. The highest occupied molecular orbital (HOMO) was determined to be 5.21 eV, calculated using the equation $E_{HOMO} = -e[E_{ox} + 4.80 - E(Fc/Fc^{+})]$. The lowest unoccupied molecular orbital (LUMO) was found to be 3.63 eV, derived from $E_{LUMO} = E_{HOMO} - E_g$. Fig. 6b shows the energy level diagram of $MAPbI_3$ perovskite and SPS-PPY-TT HTM molecules. The small HOMO band edge difference (0.22 eV) between the perovskite layer and SPS-PPY-TT enhances hole transfer and reduces associated voltage losses. Similarly, SPS-PPY-TT exhibits a higher LUMO level compared to the perovskite layer, which can serve as an electron-blocking layer and prevent charge recombination. Furthermore, using optical and electrochemical data, the change in Gibbs free energy was calculated to assess the thermodynamic feasibility of charge separation and recombination events as a function of solvent polarity, aiding in the construction of the Jablonski energy diagram. The change in free energy for these processes was determined using Rehm–Weller equations.[58] As shown in Fig. 6c, regardless of the excitation wavelength, the singlet excited state of ZnP produces radical ion pairs in *o*-DCB.

Photovoltaic performance

The planar PSC devices were fabricated using SPS-PPY-TT as a dopant-free HTM with the device structure of FTO/SnO_2/$CH_3NH_3PbI_3$/(SPS-PPY-TT/Spiro-OMeTAD)/Au. The photovoltaic performance of SPS-PPY-TT was compared with the well-known Spiro-OMeTAD HTM as a reference device. Fig. S12 shows the top-view field emission scanning electron microscopy (FESEM) images of $MAPbI_3$, Spiro-OMeTAD, and SPS-PPY-TT, respectively. The perovskite layer exhibited a smooth surface with large grains. Also, perovskite coated with Spiro-OMeTAD and SPS-PPY-TT shows similar morphology with full coverage over the perovskite active layer. Fig. 7a represents the current density–voltage (J–V) curves of the PSCs fabricated using SPS-PPY-TT and Spiro-OMeTAD as the HTM, measured at forward and reverse bias under AM 1.5 G conditions, and the corresponding photovoltaic data are summarized in Table 2.

The planar PSCs made with SPS-PPY-TT as the HTM showed a PCE of 15.29%, with an open-circuit voltage (V_{OC}) of 1.08 V, a short-circuit current density (J_{SC}) of 20.51 mA cm^{-2}, and a fill factor (FF) of 68.86% under reverse bias. Under forward bias, a PCE of 15.00%, V_{OC} of 1.07 V, J_{SC} of 20.49 mA cm^{-2}, and FF of 67.89% were observed. Under the same measurement conditions, the PSC device made with Spiro-OMeTAD as the HTM showed PCEs of 16.62% under reverse bias and 16.42% under forward bias. The hysteresis index (HI) [HI = ($PCE_{reverse}$ – $PCE_{forward}$)/$PCE_{reverse}$] was measured for both PSC devices, fabricated with SPS-PPY-TT and Spiro-OMeTAD. The Spiro-OMeTAD device exhibited an HI of 0.012, slightly lower than that of the SPS-PPY-TT device (HI = 0.018). Fig. 7b displays the external quantum efficiency (EQE) spectra of Spiro-OMeTAD and SPS-PPY-TT HTMs. Both PSC devices show broad spectra from 300 to 800 nm with high EQE values of 87% at 591 nm and 86% at 507 nm, respectively.

Furthermore, we have performed thermal analysis of SPS-PPY-TT to understand its thermal behavior, which is one of the essential factors for the durability of the PSC device. The thermal analysis suggests that the present SPS-PPY-TT is stable up to 200 °C (Fig. S14).

Pump-probe studies to probe CS

The data discussed so far are indicative of the occurrence of photo-induced electron transfer in the newly assembled donor–acceptor system. To observe and gather kinetic information about this phenomenon, femtosecond transient absorption (fs-TA) studies were performed in *o*-DCB. As shown in Fig. 8a, when the compound SPS-PPY-TT was excited at 466 nm, an immediate formation of the ^{1}ZnP* moiety was detected at 541, 772, and 1121 nm.

Additionally, a strong negative signal appeared at 665 and 729 nm, attributable to ground state bleaching (GSB), and the peak at 833 nm might be due to stimulated emission (SE). The intensity of the signal at 1121 nm began to decrease as a new

Table 2 Photovoltaic performance of SPS-PPY-TT and Spiro-OMeTAD-based PSCs

Device	V_{OC} (V)	J_{SC} (mA cm^{-2})	FF (%)	PCE (%)	R_S [Ω cm^2]	R_{SH} [Ω cm^2]	Hysteresis
Spiro-OMeTAD-reverse	1.15	20.03	71.95	16.62	5.359	4124	0.012
Spiro-OMeTAD-forward	1.15	19.98	71.44	16.42	5.582	100 860	
SPS-PPY-TT-reverse	1.08	20.51	68.86	15.29	2.9023	1197	0.018
SPS-PPY-TT-forward	1.07	20.49	67.89	15.00	2.963	1131.55	

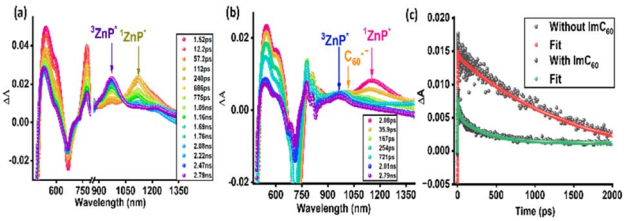

Fig. 8 Fs-TA data at the indicated delay times for (a) SPS-PPY-TT and (b) SPS-PPY-TT: ImC$_{60}$, and (c) single wavelength decay analysis at 1130 nm with and without ImC$_{60}$ after exciting the samples at 466 nm.

peak emerged at 972 nm, indicating the formation of triplet excited species, ^{3}ZnP*. To determine the lifetime of ^{1}ZnP*, a single-wavelength decay analysis was performed, revealing a lifetime of 1556 ps. The decay profile from this analysis is shown in Fig. 8c. Next, identical studies were conducted for SPS-PPY-TT:ImC$_{60}$. In this case, the decay of the excited state absorption (ESA) signal at 1145 nm resulted in the formation of a charge-separated (CS) state, confirmed by a new broad peak at 1010 nm, well known for the formation of ImC$_{60}^{\bullet-}$.[57] This peak could be a mixture of radical ion pairs, as a new signal emerged in the same region during spectroelectrochemical studies conducted to locate the site of radical cation formation. The lifetime of the ESA signal at 1145 nm was significantly quenched, indicating strong electron transfer in this system.[57–59]

Single-wavelength analysis of this peak produced a lifetime of 362 ps. Ultimately, the rate of CS (k_{CS}) was calculated from the decay curves of the singlet ESA peak in the presence and absence of ImC$_{60}$, yielding 2×10^9 s^{-1}.

Next, a nanosecond transient absorption (ns-TA) experiment was performed to identify the lifetime of the long-lived triplet species. As shown in Fig. 9a, two intense peaks appeared at 997 and 1257 nm for SPS-PPY-TT, with a lifetime of 110 μs determined from decay curves (Fig. 9c). Similarly, in the presence of ImC$_{60}$, the same spectral features were observed, with peaks at 997 and 1257 nm and a lifetime of 89 μs. The minimal quenching of this lifetime strongly suggests that the presence of ImC$_{60}$ does not influence the formation of ^{3}ZnP* (likely from unbonded ZnP), which is directly produced from ^{1}ZnP*, rather than resulting from charge recombination.

Furthermore, the samples were irradiated at 760 nm, and the results are shown in Fig. 10. The spectral features slightly

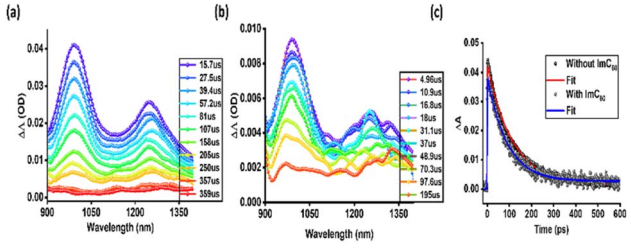

Fig. 9 Ns-TA data at the indicated delay times for (a) SPS-PPY-TT and (b) SPS-PPY-TT:ImC$_{60}$, and (c) single wavelength decay analysis at 997 nm with and without ImC$_{60}$ after exciting the compounds at 466 nm in *o*-DCB.

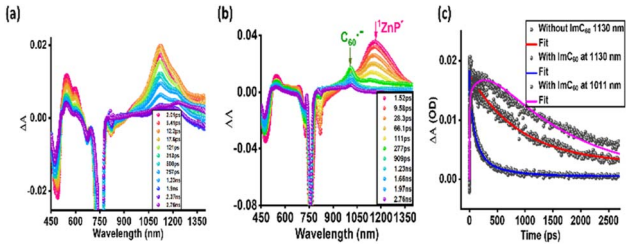

Fig. 10 Fs-TA data at the indicated delay times for (a) SPS-PPY-TT and (b) SPS-PPY-TT:ImC$_{60}$, and (c) single wavelength decay analysis at the indicated wavelength with and without ImC$_{60}$ after exciting the compounds at 760 nm in *o*-DCB.

differed from those observed when excited at 466 nm. Fig. 10a displays the fs-TA spectra of SPS-PPY-TT, where intense bands, representing ^{1}ZnP*, appeared at 544, 600, and 1125 nm. A decay fit at 1125 nm indicated that this signal lasted for 916 ps, as shown in Fig. 10c. The same experiment was then repeated after adding ImC$_{60}$, creating a new signal at 1011 nm, responsible for the formation of radical ion pairs, and causing a significant reduction in the lifetime of ^{1}ZnP* (Fig. 10b). Fig. 10c represents a single decay profile obtained at 1130 nm to assess the lifetime, which was found to be 522 ps. Based on the quenching of this lifetime, the k_{CS} was determined to be 0.9×10^9 s^{-1}. Eventually, the new peak at 1011 nm was further analysed to calculate the k_{CS} and the rate of charge recombination (k_{CR}). It yielded k_{CS} and k_{CR} values of 3.7×10^9 and 6.4×10^8 s^{-1}, respectively, and the ratio of k_{CS}/k_{CR} was found to be 5.8 from these analyses. A lower ratio of these constants could result from a greater distance between the fullerene and porphyrin entity due to the axial coordination, which can also diminish the electronic overlap between orbitals. Importantly, the extended lifetime of the radical ion pairs, as revealed by transient measurements, suggests suppressed recombination, directly contributing to the improved efficiency of the device.

Conclusions

In summary, we demonstrated an effective approach to design, synthesize, and employ the porphyrin and hexylthieno[3,2-*b*] thiophene (TT)-based hole transporting material for high-performance and stable PSCs. The structurally simple and easily accessible zinc porphyrin material, denoted as SPS-PPY-TT, can be prepared in high yields. The incorporation of the ethyne bridge and FBDT as π-spacer units between the porphyrin and TT units can strongly influence the energy levels of SPS-PPY-TT. Additionally, it enhances the planarity of SPS-PPY-TT by initiating higher π-conjugation, thereby increasing charge transport properties. The n-hexyl-substituted TT unit, as a methoxy-free donor, can improve the molecular stacking, solubility, and charge transport properties of SPS-PPY-TT. The planar PSC device fabricated with SPS-PPY-TT as the HTM shows the best PCE of 15.29%, while a PCE of 16.62% was observed for the Spiro-OMeTAD-based device. The comparable PCE of SPS-PPY-TT to high-cost Spiro-OMeTAD indicates that SPS-PPY-TT is the best alternative for fabricating low-cost and

high-efficiency PSCs. Eventually, the same system, consisting of ImC_{60}, was explored to observe the electron transfer mechanism upon photoexcitation. A series of experiments, including optical spectroscopy, electrochemical, and spectroelectrochemical studies, was employed to demonstrate this phenomenon. In addition, theoretical studies were also performed to support experimental observations, confirming the directionality of electron transfer from the porphyrin moiety to fullerene. Finally, transient studies provided conclusive evidence of the formation of radical ion pairs.

Conflicts of interest

The authors declare no conflicts of interest.

Data availability

All the data supporting this article have been included in the supplementary information (SI). Supplementary information is available. See DOI: https://doi.org/10.1039/d5el00203f.

Acknowledgements

This work was financially supported by the National Science Foundation (Grant No. 2345836 to FD). The computational work was completed at the Holland Computing Center of the University of Nebraska, which receives support from the Nebraska Research Initiative. MN thanks CSIR for a senior research fellowship, and LG acknowledges the DST-Solar Challenge Award (DST/ETC/CASE/RES/2023/05(C)/(G)) for funding this work. We thank the Director CSIR-IICT for support (IICT/Pubs./2025/279).

References

1 A. Jegorovė, J. Xia, M. Steponaitis, M. Daskeviciene, V. Jankauskas, A. Gruodis, E. Kamarauskas, T. Malinauskas, K. Rakstys, K. A. Alamry, V. Getautis and M. K. Nazeeruddin, *Chem. Mater.*, 2023, **35**, 5914–5923.
2 P. Yan, D. Yang, H. Wang, S. Yang and Z. Ge, *Energy Environ. Sci.*, 2022, **15**, 3630–3669.
3 G. B. Adugna, S. Y. Abate, W.-T. Wu and Y.-T. Tao, *ACS Appl. Mater. Interfaces*, 2021, **13**, 25926–25936.
4 J. J. Yoo, G. Seo, M. R. Chua, T. G. Park, Y. Lu, F. Rotermund, Y.-K. Kim, C. S. Moon, N. J. Jeon, J.-P. Correa-Baena, V. Bulović, S. S. Shin, M. G. Bawendi and J. Seo, *Nature*, 2021, **590**, 587–593.
5 D. Khan, X. Liu, G. Qu, A. R. Nath, P. Xie and Z.-X. Xu, *Small*, 2023, **19**, 2205926.
6 X. Yu, D. Gao, Z. Li, X. Sun, B. Li, Z. Zhu and Z. Li, *Angew. Chem., Int. Ed.*, 2023, **62**, e202218752.
7 X. Wu, D. Gao, X. Sun, S. Zhang, Q. Wang, B. Li, Z. Li, M. Qin, X. Jiang, C. Zhang, Z. Li, X. Lu, N. Li, S. Xiao, X. Zhong, S. Yang, Z. Li and Z. Zhu, *Adv. Mater.*, 2023, **35**, 2208431.
8 F. M. Rombach, S. A. Haque and T. J. Macdonald, *Energy Environ. Sci.*, 2021, **14**, 5161–5190.
9 Z. Deng, M. He, Y. Zhang, F. Ullah, K. Ding, J. Liang, Z. Zhang, H. Xu, Y. Qiu, Z. Xie, T. Shan, Z. Chen, H. Zhong and C.-C. Chen, *Chem. Mater.*, 2021, **33**, 285–297.
10 B. Xu, D. Bi, Y. Hua, P. Liu, M. Cheng, M. Grätzel, L. Kloo, A. Hagfeldt and L. Sun, *Energy Environ. Sci.*, 2016, **9**, 873–877.
11 L. Vaghi and F. Rizzo, *Sol. RRL*, 2023, **7**, 2201108.
12 J. Xu, Q. Xiong, X. Huang, P. Sun, Q. Zhou, Y. Du, Z. Zhang and P. Gao, *Small*, 2023, **19**, 2206435.
13 R. Hussain, M. Adnan, K. Atiq, M. Usman Khan, Z. H. Farooqi, J. Iqbal and R. Begum, *Sol. Energy*, 2023, **253**, 187–198.
14 M. Kishore, D. J. Vindo, Ch. Prabhakar, G. Rambabu and P. Someshwar, *Org. Electron.*, 2025, **136**, 107153.
15 A. Cubin and H. Jianhui, *Acc. Mater. Res.*, 2022, **3**, 540–551.
16 C. Wang, Q. Xiong, Z. Zhang, L. Meng, F. Li, L. Yang, X. Wang, Q. Zhou, W. Fan, L. Liang, S.-Y. Lien, X. Li, J. Wu and P. Gao, *ACS Appl. Mater. Interfaces*, 2022, **14**, 12640–12651.
17 L. Liang, N. Shibayama, H. Jiang, Z. Zhang, L. Meng, L. Zhang, C. Wang, N. Zhao, Y. Yu, S. Ito, J. Wu, J. Chen and P. Gao, *J. Mater. Chem. A*, 2022, **10**, 3409–3417.
18 B. Yadagiri, T. H. Chowdhury, Y. He, R. Kaneko, A. Islam and S. P. Singh, *Mater. Chem. Front.*, 2021, **5**, 7276–7285.
19 M. Gurulakshmi, G. Ramesh, A. Jaker, K. Susmitha, B. S. Narendra, Ch. Prabhakar, P. Someshwar and M. Raghavender, *Sol. Energy*, 2021, **226**, 501–512.
20 Y. Cao, Y. Li, T. Morrissey, B. Lam, B. O. Patrick, D. J. Dvorak, Z. Xia, T. L. Kelly and C. P. Berlinguette, *Energy Environ. Sci.*, 2019, **12**, 3502–3507.
21 K. Narayanaswamy, B. Yadagiri, T. H. Chowdhury, T. Swetha, A. Islam, V. Gupta and S. P. Singh, *Chem.–Eur. J.*, 2019, **25**, 16320–16327.
22 R. Azmi, U.-H. Lee, F. T. A. Wibowo, S. H. Eom, S. C. Yoon, S.-Y. Jang and I. H. Jung, *ACS Appl. Mater. Interfaces*, 2018, **10**, 35404–35410.
23 F. Arjmand, S. J. Fatemi, S. Maghsoudi and A. Naeimi, *J. Mater. Res. Technol.*, 2022, **16**, 1008–1020.
24 S. H. Kang, C. Lu, H. Zhou, S. Choi, J. Kim and H. K. Kim, *Dyes Pigm.*, 2019, **163**, 734–739.
25 K. Devulapally, T. H. Chowdhury, Y. He, M. N. Rajesh, S. Prasanthkumar, A. Islam and L. Giribabu, *J. Photochem. Photobiol.*, 2023, **16**, 100188.
26 H.-H. Chou, Y.-H. Chiang, Y.-H. Chen, C.-J. Guo, H.-Y. Zuo, W.-T. Cheng, P.-Y. Lin, Y.-Y. Chiu, P. Chen and C.-Y. Yeh, *Sol. RRL*, 2020, **4**, 2000119.
27 B. Yadagiri, K. Narayanaswamy, S. Revoju, B. Eliasson, G. D. Sharma and S. P. Singh, *J. Mater. Chem. C*, 2019, **7**, 709–717.
28 C. McDowell, K. Narayanaswamy, B. Yadagiri, T. Gayathri, M. Seifrid, R. Datt, S. M. Ryno, M. C. Heifner, V. Gupta, C. Risko, S. P. Singh and G. C. Bazan, *J. Mater. Chem. A*, 2018, **6**, 383–394.
29 J. S. Lee, S. K. Son, S. Song, H. Kim, D. R. Lee, K. Kim, M. J. Ko, D. H. Choi, B. Kim and J. H. Cho, *Chem. Mater.*, 2012, **24**, 1316–1323.
30 Y. Wang, Q. Liao, J. Chen, W. Huang, X. Zhuang, Y. Tang, B. Li, X. Yao, X. Feng, X. Zhang, M. Su, Z. He, T. J. Marks,

A. Facchetti and X. Guo, *J. Am. Chem. Soc.*, 2020, **142**, 16632–16643.
31 D. K. Dogutan and D. G. Nocera, *Acc. Chem. Res.*, 2019, **52**, 3143–3148.
32 W. Ong, *ACS Appl. Mater. Interfaces*, 2019, **11**, 5579–5580.
33 S. Y. Reece, J. A. Hamel, K. Sung, T. D. Jarvi, A. J. Esswein, J. J. H. Pijpers and D. G. Nocera, *Science*, 2011, **334**, 645–648.
34 M. G. Walter, E. L. Warren, J. R. McKone, S. W. Boettcher, Q. Mi, E. A. Santori and N. S. Lewis, *Chem. Rev.*, 2010, **110**, 6446–6473.
35 D. G. Nocera, *Acc. Chem. Res.*, 2012, **45**, 767–776.
36 D. Gust, T. A. Moore and A. L. Moore, *Faraday Discuss.*, 2012, **155**, 9–26.
37 C. Sebastiano, N. Francesco, L. Guiseppina, S. Scolastica, S. Antonio, A. Antonio and P. Fausto, *Phys. Chem. Chem. Phys.*, 2023, **25**, 1504–1512.
38 H. Imahori, *Bull. Chem. Soc. Jpn.*, 2023, **96**, 339–352.
39 A. Yahagh, R. R. Kaswan, S. Kazemi, P. A. Karr and F. D'Souza, *Chem. Sci.*, 2024, **15**, 906–913.
40 S. Nenavath, N. Duvva, R. R. Kaswan, G. N. Lim, F. D'Souza and L. Giribabu, *J. Phys. Chem. A*, 2023, **127**, 6779–6790.
41 S. Fukuzumi, Y.-M. Lee and W. Nam, *Tetrahedron*, 2020, **76**, 131024.
42 N. Zarrabi, N. Holzer, G. N. Lim, C. O. Obondi, A. van der Est, F. D'Souza and P. K. Poddutoori, *J. Porphyrins Phthalocyanines*, 2022, **26**, 407–417.
43 S. A. Vail, P. J. Krawczuk, D. M. Guldi, A. Palkar, L. Echegoyen, J. P. C. TomØ, M. A. Fazio and D. I. Schuster, *Chem.–Eur. J.*, 2005, **11**, 3375–3388.
44 A. L. Schumacher, A. S. D. Sandanayaka, J. P. Hill, K. Ariga, P. A. Karr, Y. Araki, O. Ito and F. D'Souza, *Chem.–Eur. J.*, 2007, **13**, 4628–4635.
45 A. Garai, M. Kumar, W. Sinha, S. Chatterjee, C. S. Purohit, T. Som and S. Kar, *RSC Adv.*, 2014, **4**, 64119–64127.
46 F. D'Souza, P. M. Smith, M. E. Zandler, A. L. McCarty, M. Itou, Y. Araki and O. Ito, *J. Am. Chem. Soc.*, 2004, **126**, 7898–7907.
47 A. Bagaki, H. B. Gobeze, G. Charalambidis, A. Charisiadis, C. Stangel, V. Nikolaou, A. Stergiou, N. Tagmatarchis, F. D'Souza and A. G. Coutsolelos, *Inorg. Chem.*, 2017, **56**, 10268–10280.
48 N. Zarrabi, C. O. Obondi, G. N. Lim, S. Seetharaman, B. G. Boe, F. D'Souza and P. K. Poddutoori, *Nanoscale*, 2018, **10**, 20723–20739.
49 S. Kazemi, A. Z. Alsaleh, P. A. Karr and F. D'Souza, *J. Am. Chem. Soc.*, 2024, **146**, 13509–13518.
50 F. D'Souza, S. Gadde, D. M. Islam, C. A. Wijesinghe, A. L. Schumacher, M. E. Zandler, Y. Araki and O. Ito, *J. Phys. Chem. A*, 2007, **111**, 8552–8560.
51 N. V. Krishna, J. V. S. Krishna, S. P. Singh, L. Giribabu, L. Han, I. Bedja, R. K. Gupta and A. Islam, *J. Phys. Chem. C*, 2017, **121**, 6464–6477.
52 R. R. Kaswan, S. Washburn, U. Oji, H. Wang and F. D'Souza, *Chem.–Eur. J.*, 2025, **31**, e202404165.
53 F. D'Souza, P. M. Smith, L. Rogers, M. E. Zandler, D.-M. Shafiqul, Y. Araki and O. Ito, *Inorg. Chem.*, 2006, **45**, 5057–5065.
54 H. A. Benesi and J. H. Hildebrand, *J. Am. Chem. Soc.*, 1949, **71**, 2703–2707.
55 M. J. Frisch, G. W. Trucks, H. B. Schlegel, G. E. Scuseria, M. A. Robb, J. R. Cheeseman, G. Scalmani, V. Barone, G. A. Petersson, H. Nakatsuji, X. Li, M. Caricato, A. V. Marenich, J. Bloino, B. G. Janesko, R. Gomperts, B. Mennucci, H. P. Hratchian, J. V. Ortiz, A. F. Izmaylov, J. L. Sonnenberg, D. Williams-Young, F. Ding, F. Lipparini, F. Egidi, J. Goings, B. Peng, A. Petrone, T. Henderson, D. Ranasinghe, V. G. Zakrzewski, J. Gao, N. Rega, G. Zheng, W. Liang, M. Hada, M. Ehara, K. Toyota, R. Fukuda, J. Hasegawa, M. Ishida, T. Nakajima, Y. Honda, O. Kitao, H. Nakai, T. Vreven, K. Throssell, J. A. Montgomery, J. E. Peralta Jr, F. Ogliaro, M. J. Bearpark, J. J. Heyd, E. N. Brothers, K. N. Kudin, V. N. Staroverov, T. A. Keith, R. Kobayashi, J. Normand, K. Raghavachari, A. P. Rendell, J. C. Burant, S. S. Iyengar, J. Tomasi, M. Cossi, J. M. Millam, M. Klene, C. Adamo, R. Cammi, J. W. Ochterski, R. L. Martin, K. Morokuma, O. Farkas, J. B. Foresman and D. J. Fox, *GAUSSIAN 16 (Revision A.03)*, Gaussian Inc., Wallingford, CT, 2016.
56 R. R. Kaswan, D. Molina, L. Ferrer-López, J. Ortiz, P. A. Karr, Á. Sastre-Santos and F. D'Souza, *Angew. Chem., Int. Ed.*, 2025, **64**, e202502516.
57 M. Wazid, Yo. Rout, A. Z. Alsaleh, R. R. Kaswan, R. Misra and F. D'Souza, *Chem. Commun.*, 2025, **61**, 6803–6806.
58 D. Rehm and A. Weller, *Isr. J. Chem.*, 1970, **7**, 259–276.
59 R. R. Kaswan, D. R. Subedi, R. Reid and F. D'Souza, *Chem.–Asian J.*, 2025, e70222.